An Improved Hydrometeor Detection Method for Millimeter-Wavelength Cloud Radar

Ge Jinming[1], Zhu Zeen[1], Zheng Chuang[1], Xie Hailing[1], Zhou Tian[1], Huang Jianping[1], and Fu Qiang [1,2]

[1]Key Laboratory for Semi-Arid Climate Change of the Ministry of Education and College of Atmospheric Sciences, Lanzhou University, Lanzhou, 730000, PRC

[2]Department of Atmospheric Sciences, University of Washington, Seattle, WA, 98105, USA

December, 2016

Abstract

A new method is proposed to distinguish clouds and other hydrometeors from noise in cloud radar observations. A noise reduction scheme that can reduce the noise distribution to a narrow range is proposed in our method in order to recognize more weak signal clouds. A spatial filter with central weighting, which is used in current cloud radar hydrometeor detection algorithms, is also involved in our method to examine radar return for significant levels of signals. "Square clouds" were constructed to test the two schemes. We applied our method to six months of cloud radar observations and compared the results with those obtained by applying the U.S. Department of Energy (DOE) Atmospheric Radiation Measurements (ARM) program operational algorithm. It was found that our method has significant advantages in recognizing clouds with weak signal and reducing the rates of both failed negative and false positive hydrometeor identifications in simulated clouds.

1. Introduction

Clouds, which are composed of liquid water droplets, ice crystals or both, cover about two-thirds of the earth surface at any time [e.g., *King et al.*, 2013]. By reflecting solar radiation back to the space (the albedo effect) and trapping thermal radiation emitted by the Earth surface and the lower troposphere (the greenhouse effect), clouds strongly modulate the radiative energy budget in the climate system [e.g., *Fu et al.*, 2002; *Huang et al.*, 2007; *Huang et al.*, 2006a; *Huang et al.*, 2006b; *Ramanathan et al.*, 1989; *Su et al.*, 2008]. Clouds are also a vital component of water cycle by connecting the water-vapor condensation and precipitation. Despite the importance of clouds in the climate system, they are difficult to represent in climate models [*Williams and Webb*, 2009], which causes the largest uncertainty in the predictions of climate change by general circulation models (GCMs) [e.g., *Randall*, 2007; *Stephens*, 2005; *Williams and Webb*, 2009].

Cloud formation, evolution and distribution are governed by complex physical and dynamical processes on a wide range of scales from synoptic motions to turbulence [*Bony et al.*, 2015]. Unfortunately, the processes that occur on smaller spatial scales than a GCM grid box cannot be resolved by current climate models, and the coupling between large scale fluctuations and cloud microphysical processes are not well understood [e.g., *Huang et al.*, 2006b; *Mace et al.*, 1998; *Yan et al.*, 2015; *Yuan et al.*, 2006]. Moreover, the cloud horizontal inhomogeneity and vertical overlap are not resolved by GCMs [*Barker*, 2000; *Barker and Fu*, 2000; *Fu et al.*, 2000a; *Fu et al.*, 2000b; *Huang et al.*, 2005; *Li et al.*, 2015]. To better understand cloud processes for improving their parameterization in climate models and revealing their evolution in response to climate change, long-term continuous observations of cloud fields in terms of both macro- and micro-physical properties are essential [e.g., *Ackerman and Stokes*, 2003; *Sassen and Benson*, 2001; *Thorsen et al.*, 2011; *Wang and Sassen*, 2001].

Millimeter-wavelength Cloud Radars (MMCRs) can resolve cloud vertical structure for their occurrences and microphysical properties [e.g., *Clothiaux et al.*, 1995; *Kollias et al.*, 2007a; *Mace et al.*, 2001]. The wavelengths of MMCRs are shorter than those of weather radars making them sensitivity to cloud droplets and ice crystals and can penetrate multiple cloud layers [e.g., *Kollias et al.*, 2007a]. Because of their outstanding advantages for cloud research, millimeter-wavelength radars have been deployed on various research platforms including the first space-borne millimeter-wavelength Cloud Profiling Radar (CPR) onboard the CloudSat [*Stephens et al.*, 2002]. Ground-based cloud radar are operated at the U.S. Department of Energy's Atmospheric Radiation Program (ARM) observational sites (used to MMCRs, now are replaced with a new generation of Ka band Zenith Radar (KAZR)) [e.g., *Ackerman and Stokes*, 2003; *Clothiaux et al.*, 2000; *Clothiaux et al.*, 1999; *Kollias et al.*, 2007b; *Protat et al.*, 2011] and in Europe [*Illingworth et al.*, 2007; *Protat et al.*, 2009]. In July 2013, KAZR was deployed in China at the Semi-Arid Climate and Environment Observatory of Lanzhou University (SACOL) site (latitude: 35.946°N; longitude: 104.137°E; altitude: 1.97 km) [*Huang et al.*, 2008]，providing an opportunity to observe and reveal the detailed structure of the mid-latitude clouds over East Asia semi-arid regions.

Before characterizing the cloud physical properties from the cloud radar return signal, we first need to distinguish and extract the hydrometeor signals from the background noise (i.e. cloud mask). A classical cloud mask method was developed in Clothiaux et al.[2000; 1995] by analyzing the strength and significance of returned signals. This method consists of two main steps. First any power in a range gate that is greater than a mean value of noise plus one standard deviation is selected as a bin containing potential hydrometer signal. Second, a spatial-time coherent filter is created to estimate the significance level of the potential hydrometer bin signal to be real. This cloud mask algorithm is operationally used for the ARM MMCRs data analysis and was later adopted to the CPR onboard the CloudSat [*Marchand et al.*, 2008].

It is recognized that by visually examining a cloud radar return image, one can easily tell where the return power is likely to be caused by hydrometeors and where the power is just from noise. This ability of human eye on extracting and analyzing information from an image has been broadly studied in image processing and computer vision, and a number of mathematical methods for acquiring and processing information from images have been developed, including some novel algorithms for noise reduction and edge detection [*Canny*, 1986; *He et al.*, 2013; *Marr and Hildreth*, 1980; *Perona and Malik*, 1990]. In this paper we develop a new cloud mask method for cloud radar by noticing that removing noise from signal and identifying cloud boundaries are the essential goals of cloud mask. This method reduces the radar noise while preserving cloud edges by employing the bilateral filtering that is widely used in the image processing [*Tomasi and Manduchi*, 1998]. The power weighting probability method proposed by Marchand et al.[2008] is also adopted in our method to prevent the cloud corners from being removed. It is found that our improved hydrometeor detection algorithm is more efficient in terms of reducing false positives and negatives as well as identifying cloud features with weak signals such as thin cirrus clouds.

The KAZR deployed at the SACOL is described in section 2 and the new cloud mask algorithm is introduced in section 3. The applications of the new scheme to both hypothetical and observed cloud fields including a comparison with previous schemes are shown in section 4. Summary and conclusions are given in section 5.

2. The KAZR Radar

The SACOL KAZR, built by ProSensing Inc. of Amherst, MA, is a zenith-pointing cloud radar operating at approximately 35 GHz for the dual-polarization measurements of Doppler spectra. The main purpose of the KAZR is to provide vertical profiles of clouds by measuring the first three Doppler moments: reflectivity, radial Doppler velocity, and spectra width. The linear depolarization ratio [*Marr and Hildreth*, 1980] can be computed from the ratio of cross-polarized reflectivity to co-polarized reflectivity.

The SACOL KAZR has a transmitter with a peak power of 2.2 kw and two modes working at separate frequencies. One is called "chirp" mode that uses a linear-FM (frequency modulation) pulse compression to achieve high radar sensitivity of about -65 dBZ at 5 km altitude. The minimum altitude (or range) that can be detected in chirp mode is approximately 1 km AGL. To view clouds below 1 km, a short pulse or "burst mode" pulse is transmitted at a separate frequency just after transmission of the chirp pulse. This burst mode pulse allows clouds as low as 200 m to be measured. The chirp pulse is transmitted at 34.890 GHz while the burst pulse is transmitted at 34.830 GHz. These two waveforms are separated in the receiver and processed separately.

The pulse length is approximately 300 ns (giving a range resolution of 45 m), while the digital receiver samples the return signal every 30 m. The interpulse period is 208.8 μs, the number of coherent averages is 1, and the number of the fast Fourier transform (FFT) points is currently set to 512. An unambiguous range is thus 31.29 km, an unambiguous velocity is 10.29 m/s, and a velocity resolution of is 0.04m/s. The signal dwell time is 4.27s. These operational parameters are set for the purpose of having enough radar sensitivity and accurately acquiring reflectivities of hydrometeors. In this study, we mainly use radar observed reflectivity (dBZ) data to test our new hydrometeor detection method.

3. Hydrometeor detection algorithm

The basic assumption in the former cloud mask algorithms [*Clothiaux et al.*, 1995; *Marchand et al.*, 2008] is that the random noise power follows the normal distribution. In this study, several clear sky cases in all seasons from the KAZR observations were firstly selected to analyze its background noise power distributions (Fig.1). As demonstrated in Fig.1a for a clear-sky case during 0000 to 1200 UTC on January 21st, 2014, the noise power estimated from the top 30 range gates, which includes both internal and external sources[*Fukao and Hamazu*, 2014], has an apparent non-Gaussian distribution with a positive skewness of 1.40. The signal-to-noise ratio (SNR) is defined as:

$$\mathrm{SNR} = 10\log(\frac{P_s}{P_n}) \quad (1)$$

where P_s is the power received at each range gate in a profile, P_n is the mean noise power that is estimated by averaging the return power in the top 30 range gates which are between 16.8 and 17.7 km AGL. Since this layer is well above the tropopause, few atmospheric hydrometeors existing in this layer can scatter enough power back to achieve the radar sensitivity. Figure 1a shows that the SNRs for clear skies closely follow a Gaussian distribution. Instead of using radar received power, the SNR is used to estimate the background noise level and taken as the input to the cloud mask procedure since the SNR satisfies the assumption of a normally distributed noise and in our method the chance for the central range gate to be a noise or a potential signal relies on calculating the probability for a given range of SNR values based on the Gaussian distribution. Note that the mean value of the SNR for the noise power is not zero, but a small negative value of about -0.3. This is because the mean of the noise power is larger than its the median due to its positive skewed distribution. It is further noted that the distribution of SNR and its mean for the top 30 range gates are the same as those from the lower atmosphere.

The SNR value is treated as the brightness of a pixel in an image $f(x, y)$ in our hydrometeor detection method. In an image processing, the random noise can be smoothed out by using a low pass filter, which gives a new value for a pixel of an image by averaging with neighboring pixels [*Tomasi and Manduchi*, 1998]. The cloud signals are highly correlated in both space and time and have more similar values in near pixels while the random noise values are not correlated. Therefore, as illustrated in Fig. 2a, this low pass filter can efficiently reduce the original radar noise represented by the green line to a narrow bandwidth (blue line) while keeping the signal preserved. By reducing the standard deviations of noise, which shrinks the overlap region of signal and noise and enhances their contrast, the weak signals (yellow area) that cannot be detected based on original noise level may become distinguished.

Based on this idea, we develop a non-iterative hydrometeor detection algorithm by applying a noise reduction and a central pixel weighting schemes. Figure 3 shows the schematic flow diagram of our method. The input SNR data set is first separated into two groups. One group with values greater than the mean background noise SNR (S_o) plus three times of its standard deviation (σ_o) are considered as the cloud features that can be confidently identified. Another group with values between S_o and $S_o + 3\sigma_o$ may potentially contain moderate ($S_o + \sigma_o < SNR \leq S_o + 3\sigma_o$) to weak ($S_o < SNR \leq S_o + \sigma_o$) cloud signals, which will further go through a noise reduction process. Here S_o and σ_o are estimated from the top 30 range gates of each five successive profiles.

The noise reduction process is mainly performed by convolving radar SNR time-height data with a low pass filter. The Gaussian Filter, which outputs a `weighted average' of each pixel and its neighborhood with the average weighted more towards the value of the central pixel (v_0), is one of the most common functions of the noise reduction filter. A 2-D Gaussian distribution kernel, shown in Fig. 2b$_1$, can be expressed as:

$$\mathrm{G}(i,j) = \frac{1}{2\pi\sigma^2}\exp\left(-\frac{i^2+j^2}{2\sigma^2}\right) \qquad (2)$$

where i and j are the indexes in a filter window which are 0 for the central pixel, and σ is standard deviation of the Gaussian distribution for the window size of the kernel.

Equation (2) is used in our study to filter the radar SNR image. Note that the convolution kernel is truncated at about three standard deviations away from the mean in order to accurately represent the Gaussian distribution. Figure 1b are the cumulative distribution functions (CDFs) of clear sky SNR by convolving the same data in Fig. 1a with four filters that have different kernel sizes (3×3, 5×5, 7×7 and 9×9 pixels) corresponding to the σ ranging from 0.5 to 2. The original SNR values are distributed from about -5 to 5. After convolving the image with the Gaussian filter, the SNR distribution can be constrained to a much narrower range. It is clear that the filter with a larger kernel size is more effective in suppressing the noise. Shown in Fig. 1c are results for a cloudy case on January 4th,2014 by applying the filter to the range gates inside the cloud but adjacent to the boundary, showing that a larger kernel size shifts the SNR farther away from the noise region. It therefore appears that increasing the standard deviation (i.e. the window size) continues reducing the noise and increasing the contrast between signal and noise more effectively. On the other hand, a larger kernel can also attenuate or blur the high frequency components of an image (e.g., the boundary of clouds) more at the same time. As shown in Fig. 1d, when the window size is increased from 3×3 (σ=0.5) to 9×9 (σ=2), the SNR distribution of the range gates that are outside the cloud but adjacent to the boundary gradually move toward larges values. This will consequently raise the risk of misidentifying cloud boundaries. To solve this problem, a bilateral filtering idea proposed by *Tomasi and Manduchi* [1998] is adopted here. Considering a sharp edge between cloudy and clear region as shown in Fig. 2b$_2$, we define a $\delta(i,j)$ function that when the central pixel is on the cloudy or clear side, gives a weighting of 1 to the similar neighboring pixels (i.e. on the same side), and 0 to the other side. After combining this δ function to the Gaussian kernel in Fig. $2b_1$, we can get a new non-linear function called bilateral kernel as shown in Fig. $2b_3$. It can be written as:

$$\mathrm{B}(i, j) = \frac{1}{2\pi\sigma^2} \exp(-\frac{i^2+j^2}{2\sigma^2}) \cdot \delta(i, j). \qquad (3)$$

Thus the bilateral kernel will reduce averaging noises with signals, and vice versa. The noise-reduced image $\mathrm{h}(\mathrm{x}, \mathrm{y})$ is produced by convolving the bilateral kernel with the input image $f(\mathrm{x}, \mathrm{y})$ as:

$$\mathrm{h}(x, y) = \mathrm{k}^{-1}(x, y) \sum_{j=-w}^{j=w} \sum_{i=-w}^{i=w} f(x+i, y+j) \cdot B(i, j) \qquad (4)$$

where $\pm$w is the bounds of the finite filter window, $\mathrm{k}^{-1}(x, y)$ is defined as $1/\sum_{j=-w}^{j=w} \sum_{i=-w}^{i=w} B(i, j)$ which is used to normalize the weighting coefficients. Since the bilateral kernel function only average the central pixel with neighbors on the same side (Fig. 2b), ideally it will preserve sharp edges of a target. We will discuss how to construct the δ function in order to group the central pixel with its neighbors later in this section. In the noise reduction process, a 5×5 window size (i.e., 25 bins in total) is specified for the low pass filter, which is empirically determined by visually comparing the cloud masks with original images. We should keep in mind that the window size is compromised since a small window size is less effective in noise reduction but a large window is not suitable for recognizing weak signals.

For performing the noise reduction with Eq. (4) in a 5x5 filter window, the number of range bins (*Ns*) with signal greater than $S_o + 3\sigma_o$ are first counted. These N_s range bins are then subtracted from the total 25 of the range bins in the filter window. Note that a noise reduction is only applied when the central pixel is among the 25-Ns bins, and the δ function is set to be zero for the Ns range bins. If the remaining 25-N_s range bins are all noises, the range bin number (N_m) with SNR greater than $S_o + \sigma_o$ should be about equal to an integral number (N_t) of 0.16×(25-N_s) where 0.16 is the probability for a remaining range bin to have a value greater than $S_o + \sigma_o$ for a Gaussian noise. Thus when N_m is equal to or smaller than N_t, all the 25-N_s range bins could only contain pure noise and/or some weak cloud signals. In this case, the δ function is set to 1 for all the 25-N_s bins. When N_m is found to be larger than N_t, the 25-N_s range bins might contain a combination of moderate signal, noise and/or some weak clouds. In this case, $S_o + \sigma_o$ is selected as a threshold to determine whether the neighboring pixels are on the same side of the central pixel. If the central pixel has a value greater than $S_o + \sigma_o$, the δ function is assigned to 1 for the 25-N_s pixels with $\text{SNR} \geq S_o + \sigma_o$, but 0 for the neighboring bins with $\text{SNR} < S_o + \sigma_o$. If the central pixel is less than $S_o + \sigma_o$, the δ function is assigned to 1 for the neighboring pixels with $\text{SNR} < S_o + \sigma_o$, but 0 for the 25-Ns bins with $\text{SNR} \geq S_o + \sigma_o$.

After picking out the strong return signals and applying the noise reduction scheme, the new background noise S_n and its standard deviation σ_n are estimated. While S_n is the same as S_o, the σ_n is significantly reduced, which is a half of σ_o. This will make it possible to identify more hydrometeors as exhibited in Fig.2a. We assign different confidence level values to the following initial cloud mask according to the SNR. 40 is first assigned to the mask of any range bins with $SNR > S_o + 3\sigma_o$ in the original input data. For the rest of the range bins after applying the noise reduction, if the $SNR >$

$S_n + 3\sigma_n$, the mask is assigned to be 30; if $S_n + 2\sigma_n < SNR \leq S_n + 3\sigma_n$, the mask is 20; if $S_n + \sigma_n < SNR \leq S_n + 2\sigma_n$, the mask is 10; and the remaining range bin mask is assigned to be 0.

To reduce both false positives (i.e. false detections) and false negatives (i.e. failed detections), the next step is to estimate whether a range gate contains significant hydrometeor. Following Clothiaux et al.[2000; 1995] and Marchand et al.[2008], a 5×5 spatial filter is used to calculate the probability of clouds and noise occurring in the 25 range gates. The probability of central pixel weighting scheme proposed by Marchand et al. [2008] is adopted, and the weighting for the central pixel is assigned according to its initial mask value. The probability is calculated by

$$p = G(L)(0.16^{N_T})(0.84^{N_0}) \quad (5)$$

where N_0 is the number of masks with zeros values, N_T is the number of masks with non-zeros values and $N_0 + N_T = 25$; G(L) is the weighting probability of the central pixel that could be a false detection where L is the significant level in the initial cloud mask [G(0)=0.84, G(10)=0.16, G(20)=0.028, G(⩾30)=0.002]. If p estimated from Eq. (5) is less than a given threshold (p_{thresh}), then the central pixel is likely to be a hydrometeor signal. The value in the cloud mask will set to be the same value as in the initial mask if it is non-zero; otherwise it will be set to 10. Likewise, if $p > p_{thresh}$, then the central pixel is likely to be noise and will be set to 0. This process is iterated 5 times for each pixel to obtain the final cloud mask.

Following Marchand et al. [2008] who well explained the logic of choosing a proper threshold, p_{thresh} is calculated as

$$p_{thresh} = (0.16^{N_{thresh}})(0.84^{25-N_{thresh}}) \quad (6)$$

Note that a smaller p_{thresh} will keep the false positives lower but increase the false negative. Herein the p_{thresh} of 5.0×10^{-12} used in Clothiaux et al.[2000], which is approximately equivalent to $N_{thresh} = 13$, is selected.

Figure 4 illustrate the main steps of our detection method by using the data from January 8th, 2014. Figure 4a is the original SNR input. Figure 4b shows the SNR distribution after the noise reduction process. One can see that the SNR is compressed to a narrow range and become much smoother than original input after the noise reduction process. This step significantly increases the contrast between signal and noise. Figure 4c indicates the range gates that potentially contain hydrometeors in the initial cloud mask. Figure 4d is the final result by applying the spatial filter.

4. Results

4.1 Detection test

To test the performance of our hydrometeor detection method, we create 7 squares of SNR with sides of 100, 50, 25, 15, 10, 5, and 3 bins to mimic the radar "time-height" observations as shown in Fig. 5. The background noise is randomly given by a Gaussian distribution with a mean S_0 and a standard deviation σ_0. The targets in panels a_1, a_2 and a_3 are set with different SNR values to represent situations in which clouds have strong, moderate and weak signals, respectively. In panel a_1, the targets signals are set to be $S_0 + 10\sigma_0$. In panel a_2, the targets signals distribute from $S_0 + \sigma_0$ to $S_0 + 3\sigma_0$ with a mean value of $S_0 + 2\sigma_0$. In panel a_3, the targets SNRs range from S_0 to $S_0 + \sigma_0$ with a mean value of $S_0 + 0.5\sigma_0$.

The three middle panels in Fig. 5 show the results after applying the noise reduction. Comparing with the input signals, we can see that the background noise is well compressed and becomes more smooth. The shapes of the square targets are all well maintained with sharp boundaries for strong and moderate signals (see panels b1 and b2). In panel b3 for weak signals, the 3-bin square target is not obvious while the other 6 squares are still distinguishable. To separate the compressed background noise from hydrometeor signals, the 5×5 spatial filter is further applied to the noise-reduced data. The three right panels in Fig.5 show the final mask results. Generally, the hydrometeor detection method can identify those targets well. Six of the seven square targets can be identified for clouds with strong and moderate SNR. The 3×3 square is missed because the small targets cannot be resolved by the 5×5 spatial filter. Since the temporal resolution of KAZR is about 4 seconds, we expect that a cloud only having 3 bins in horizontal would be rare. For the targets with weak SNR values, the 3×3 and 5×5 square targets are missed, but the rest five square targets are successfully distinguished and their boundaries are well maintained.

To further demonstrate the performance of our method to detect the hypothetical clouds in Fig.5 a1, a2, and a3, the false and failed detection rates are listed in the table 1. For strong signals, no background noise pixel is misidentified as one containing hydrometeors at level 40. Although at levels less than 40, some noise pixels around the edges of targets are identified as signals, the false detection is within 0.05%. The failed detection rate is about 0.24%. For moderate signals, the failed detection rate is still as small as 0.23%, while the false detection increases a little to 0.10% at the confidence levels below 30. The failed detection can reach up to 9.77% for weak signal at level 10, but more than 90% weak signals can be captured in our method. Note that the false positive is less than 0.01%; in other words, any range gate that is detected likely as a signal bin will have extremely high likelihood to contain hydrometeors.

The simple square clouds are also tested by using the ARM operational hydrometeor detection algorithm that does not include the noise reduction and weighting schemes. As can be seen in Fig. 6, the ARM operational algorithm can only find five of the seven square targets with strong and moderate SNR. Meanwhile without central pixel weighting, the corners of the targets become rounded and more than 2.23% of hydrometeors are missed for strong and moderate cloud cases. Without the noise reduction, none of the weak cloud signals can be detected. Comparing Fig.5 and Fig.6, it is obvious that our hydrometeor detection method can well maintain the cloud boundary, keep both false and failed detection rate as low as a few percent for strong and moderate cloud cases, and has a remarkable advantage in recognizing weak signals.

4.2 Application to the SACOL KAZR observations

Our hydrometeor detection method was then applied to the winter and summer months (Dec. in 2013, Jan., Feb., Jun., Jul. and Aug. in 2014) KAZR data at the SACOL. A micropulse lidar (MPL) transmitted at 527 nm is operated nearby the KAZR. Lidar is more sensitive to thin cirrus clouds and thus used to assess the performance of our algorithm. Figure 7 a, b & c show an one-day example of radar reflectivity, normalized backscatter and depolarization ratio of lidar, respectively. The cloud masks from our detection method and the ARM operational method without the noise reduction and the central pixel weighting are shown in Fig. 7d&e. The MPL feature mask derived by modifying the method proposed in Thorsen et al. [2015] and Thorsen and Fu [2015] is shown in Fig. 7f. The vertical and horizontal resolutions of the radar and lidar are different, and we map the observed data and derived feature mask on the same height and time coordinates for a simple comparison. A distinct thin feature layer appears at about 8 km during 1500 to 1830 UTC form the lidar observation which is clearly identified as a cirrus cloud using the depolarization ratio. The contrast between the cirrus layer and background from the KAZR observation (Fig. 7a) is very weak, and only a few range gates are identified as the ones containing hydrometeors using the method without the noise reduction and weighting (Fig. 7d). However, our cloud mask method can find more range gates (about 2.8 times of ARM's result). All these increased range bins from our method are also detected as thin cirrus by the MPL (Fig. 7f). Another apparent discrepancy exists in the low atmosphere layer. A non-negligible number of range gates at about 2 km are recognized as hydrometeor echoes by our method but mostly missed by former technique. This feature layer is also apparent in lidar observations with both relative large backscatter intensities and depolarization ratios(Fig. 7b&c). MPL recognizes this feature as an aerosol layer. In our KAZR observations, we did find some dust events that were detected by this millimeter wavelength radar (see the auxiliary Fig.1). Those hydrometeor echoes detected by our method might partly be caused by large dust particles. Although the dust is not desired for cloud mask, the appearance of those particles dose prove the ability of our method on recognizing weak signals.

The upper two panels in Fig. 8 compares the number of occurrences of the detected hydrometeor range bins from our new methods with that from the ARM operational algorithm for the six months of data. Generally, one can see that the variations of the identified hydrometeor numbers with height from the two techniques are in a good agreement. The distinct discrepancies appear at about 2 km in Winter and above 13 km in Summer where our method apparently identify more hydrometeors. To illustrate the improvements of our method and quantitatively evaluate the two schemes used in the algorithm, we plot the percent change of the detected hydrometeor bins form our method comparing with that from the ARM operational method in the lower two panels in Fig. 8. As expected from the results in the test square clouds, our method can identify more signals. The remarkable feature is that the increased percentage is over 20% at high altitude, indicating that our method can recognize more cirrus clouds. The increased percentage of hydrometeor derived only with the weighting scheme (dashed line) and with both the noise reduction and weighting schemes (solid line) are separated to demonstrates the individual contribution of the scheme to the improvement of our method. In winter , the number of the detected hydrometeors only with the weighting scheme is almost the same as that from the ARM operational method at layer from 3.5 to 9 km AGL, while this number will increase by about 5% if the noise reduction scheme is involved, indicating that some hydrometeors with weak SNR values may exit in this layer. Above and below this atmospheric layer, the increased percentage is largely determined by the weighting scheme. In summer, the two line almost overlap each other between 3.5 and 9.5 km with values below 5%, revealing that the bins found by our method in the middle atmospheric layer are mainly around the boundaries of clouds. We may infer that in summer season, clouds in middle level are usually composed of large droplets with strong SNR values. The two lines are gradually apart with height. This is because hydrometeors in the upper of troposphere are usually with smaller size and cause weak SNR values that will be effectively detected by the noise reduction scheme. Note that the confusion matrix shows that the cancellation errors can be negligible.

We also analyzed data in January July, 2014 when both KAZR and MPL observations are available, and showed the percentage of the increased detections identified by both KAZR with our method and MPL observations as compared to the total increased detections in Fig. 9. It is obviously that most of the increased detections are also detected as features by MPL. The percentage drops to a minimum of 70% at about 9 km, where the total increased cloud range bins are only about 110 and there are 35 range bins that are identified by our method not observed by MPL. Considering all the increased detections by our method, 98.6% of them are confirmed by MPL as features.

5. Summary and Discussion

Based on image noise reduction technique, we propose a new method to detect hydrometeors from cloud radar return signals. The basic idea is to treat the SNR value of each range gate as a pixel brightness and suppress the SNR distributions of noise to a narrow range by convolving with a 2-D bilateral kernel. After the noise smoothing process, a special filter with central-pixel weighting scheme is used to get the final cloud mask. The test square clouds show that there are two remarkable advantages of our method: First the noise reduction scheme of our algorithm can enhance the contrast between signal and noise, while keeping the cloud boundaries preserved and detecting more hydrometeors with weak SNR values. Second both false positive and failed negative rates for strong and moderate clouds can be reduced to acceptably small values. A comparison of radar and lidar observed case further highlight the advantage of our method in application.

Acknowledgements: This work was supported by the National Science Foundation of China (41430425, 41575016, 41521004, 41505011), China 111 project (No.B 13045), and the Fundamental Research Funds for the Central University (lzujbky-2016-k01).

Reference

Ackerman, T. P., and G. M. Stokes (2003), The Atmospheric Radiation Measurement program (vol 56, pg 38, 2003), *Physics Today*, *56*(2), 14-14.

Barker, H. W. (2000), Indirect aerosol forcing by homogeneous and inhomogeneous clouds, *Journal of Climate*, *13*(22), 4042-4049, doi:10.1175/1520-0442(2000)013<4042:iafbha>2.0.co;2.

Barker, H. W., and Q. Fu (2000), Assessment and optimization of the gamma-weighted two-stream approximation, *Journal of the Atmospheric Sciences*, *57*(8), 1181-1188, doi:10.1175/1520-0469(2000)057<1181:aaootg>2.0.co;2.

Bony, S., et al. (2015), Clouds, circulation and climate sensitivity, *Nature Geoscience*, *8*(4), 261-268, doi:10.1038/ngeo2398.

Canny, J. (1986), A COMPUTATIONAL APPROACH TO EDGE-DETECTION, *Ieee Transactions on Pattern Analysis and Machine Intelligence*, *8*(6), 679-698.

Clothiaux, E. E., T. P. Ackerman, G. G. Mace, K. P. Moran, R. T. Marchand, M. A. Miller, and B. E. Martner (2000), Objective determination of cloud heights and radar reflectivities using a combination of active remote sensors at the ARM CART sites, *Journal of Applied Meteorology*, *39*(5), 645-665, doi:10.1175/1520-0450(2000)039<0645:odocha>2.0.co;2.

Clothiaux, E. E., M. A. Miller, B. A. Albrecht, T. P. Ackerman, J. Verlinde, D. M. Babb, R. M. Peters, and W. J. Syrett (1995), AN EVALUATION OF A 94-GHZ RADAR FOR REMOTE-SENSING OF CLOUD PROPERTIES, *Journal of Atmospheric and Oceanic Technology*, *12*(2), 201-229, doi:10.1175/1520-

0426(1995)012<0201:aeoagr>2.0.co;2.

Clothiaux, E. E., K. P. Moran, B. E. Martner, T. P. Ackerman, G. G. Mace, T. Uttal, J. H. Mather, K. B. Widener, M. A. Miller, and D. J. Rodriguez (1999), The atmospheric radiation measurement program cloud radars: Operational modes, *Journal of Atmospheric and Oceanic Technology*, *16*(7), 819-827, doi:10.1175/1520-0426(1999)016<0819:tarmpc>2.0.co;2.

Fu, Q., M. Baker, and D. L. Hartmann (2002), Tropical cirrus and water vapor: an effective Earth infrared iris feedback?, *Atmospheric Chemistry and Physics*, *2*, 31-37.

Fu, Q., B. Carlin, and G. Mace (2000a), Cirrus horizontal inhomogeneity and OLR bias, *Geophysical Research Letters*, *27*(20), 3341-3344, doi:10.1029/2000gl011944.

Fu, Q., M. C. Cribb, and H. W. Barker (2000b), Cloud geometry effects on atmospheric solar absorption, *Journal of the Atmospheric Sciences*, *57*(8), 1156-1168.

Fukao, S., and K. Hamazu (2014), Radar for Meteorological and Atmospheric Observations, *Springer*.

He, K., J. Sun, and X. Tang (2013), Guided Image Filtering, *Ieee Transactions on Pattern Analysis and Machine Intelligence*, *35*(6), 1397-1409, doi:10.1109/tpami.2012.213.

Huang, J. P., J. Ge, and F. Weng (2007), Detection of Asia dust storms using multisensor satellite measurements, *Remote Sensing of Environment*, *110*(2), 186-191, doi:10.1016/j.rse.2007.02.022.

Huang, J. P., P. Minnis, B. Lin, Y. H. Yi, T. F. Fan, S. Sun-Mack, and J. K. Ayers (2006a), Determination of ice water path in ice-over-water cloud systems using combined

MODIS and AMSR-E measurements, *Geophysical Research Letters*, *33*(21), doi:10.1029/2006gl027038.

Huang, J. P., P. Minnis, B. Lin, Y. H. Yi, M. M. Khaiyer, R. F. Arduini, A. Fan, and G. G. Mace (2005), Advanced retrievals of multilayered cloud properties using multispectral measurements, *Journal of Geophysical Research-Atmospheres*, *110*(D15), doi:10.1029/2004jd005101.

Huang, J. P., Y. J. Wang, T. H. Wang, and Y. H. Yi (2006b), Dusty cloud radiative forcing derived from satellite data for middle latitude regions of East Asia, *Progress in Natural Science*, *16*(10), 1084-1089.

Huang, J. P., et al. (2008), An Overview of the Semi-arid Climate and Environment Research Observatory over the Loess Plateau, *Advances in Atmospheric Sciences*, *25*(6), 906-921, doi:10.1007/s00376-008-0906-7.

Illingworth, A. J., et al. (2007), Cloudnet - Continuous evaluation of cloud profiles in seven operational models using ground-based observations, *Bulletin of the American Meteorological Society*, *88*(6), 883-+, doi:10.1175/bams-88-6-883.

King, M. D., S. Platnick, W. P. Menzel, S. A. Ackerman, and P. A. Hubanks (2013), Spatial and Temporal Distribution of Clouds Observed by MODIS Onboard the Terra and Aqua Satellites, *Ieee Transactions on Geoscience and Remote Sensing*, *51*(7), 3826-3852, doi:10.1109/tgrs.2012.2227333.

Kollias, E. E. Clothiaux, M. A. Miller, B. A. Albrecht, G. L. Stephens, and T. P. Ackerman (2007a), Millimeter-wavelength radars - New frontier in atmospheric cloud and precipitation research, *Bulletin of the American Meteorological Society*, *88*(10), 1608-+, doi:10.1175/bams-88-10-1608.

Kollias, E. E. Clothiaux, M. A. Miller, E. P. Luke, K. L. Johnson, K. P. Moran, K. B. Widener, and B. A. Albrecht (2007b), The Atmospheric Radiation Measurement Program cloud profiling radars: Second-generation sampling strategies, processing, and cloud data products, *Journal of Atmospheric and Oceanic Technology*, *24*(7), 1199-1214, doi:10.1175/jtech2033.1.

Li, J., J. Huang, K. Stamnes, T. Wang, Q. Lv, and H. Jin (2015), A global survey of cloud overlap based on CALIPSO and CloudSat measurements, *Atmospheric Chemistry and Physics*, *15*(1), 519-536, doi:10.5194/acp-15-519-2015.

Mace, G. G., T. P. Ackerman, P. Minnis, and D. F. Young (1998), Cirrus layer microphysical properties derived from surface-based millimeter radar and infrared interferometer data, *Journal of Geophysical Research-Atmospheres*, *103*(D18), 23207-23216, doi:10.1029/98jd02117.

Mace, G. G., E. E. Clothiaux, and T. P. Ackerman (2001), The composite characteristics of cirrus clouds: Bulk properties revealed by one year of continuous cloud radar data, *Journal of Climate*, *14*(10), 2185-2203, doi:10.1175/1520-0442(2001)014<2185:tccocc>2.0.co;2.

Marchand, R., G. G. Mace, T. Ackerman, and G. Stephens (2008), Hydrometeor detection using Cloudsat - An earth-orbiting 94-GHz cloud radar, *Journal of Atmospheric and Oceanic Technology*, *25*(4), 519-533, doi:10.1175/2007jtecha1006.1.

Marr, D., and E. Hildreth (1980), THEORY OF EDGE-DETECTION, *Proceedings of the Royal Society Series B-Biological Sciences*, *207*(1167), 187-217, doi:10.1098/rspb.1980.0020.

Perona, P., and J. Malik (1990), SCALE-SPACE AND EDGE-DETECTION USING ANISOTROPIC DIFFUSION, *Ieee Transactions on Pattern Analysis and Machine Intelligence*, *12*(7), 629-639, doi:10.1109/34.56205.

Protat, A., D. Bouniol, J. Delanoe, P. T. May, A. Plana-Fattori, A. Hasson, E. O'Connor, U. Goersdorf, and A. J. Heymsfield (2009), Assessment of Cloudsat Reflectivity Measurements and Ice Cloud Properties Using Ground-Based and Airborne Cloud Radar Observations, *Journal of Atmospheric and Oceanic Technology*, *26*(9), 1717-1741, doi:10.1175/2009jtecha1246.1.

Protat, A., J. Delanoe, P. T. May, J. Haynes, C. Jakob, E. O'Connor, M. Pope, and M. C. Wheeler (2011), The variability of tropical ice cloud properties as a function of the large-scale context from ground-based radar-lidar observations over Darwin, Australia, *Atmospheric Chemistry and Physics*, *11*(16), 8363-8384, doi:10.5194/acp-11-8363-2011.

Ramanathan, V., R. D. Cess, E. F. Harrison, P. Minnis, B. R. Barkstrom, E. Ahmad, and D. Hartmann (1989), CLOUD-RADIATIVE FORCING AND CLIMATE - RESULTS FROM THE EARTH RADIATION BUDGET EXPERIMENT, *Science*, *243*(4887), 57-63, doi:10.1126/science.243.4887.57.

Randall, D. A., R.A. Wood, S. Bony, R. Colman, T. Fichefet, J. Fyfe, V. Kattsov, A. Pitman, J. Shukla, J. Srinivasan, R.J. Stouffer, A. Sumi and K.E. Taylor (2007), Cilmate Models and Their Evaluation. In: Climate Change 2007: The Physical Science Basis, *Contribution of Working Group I to the Fourth Assessment Report of the*

Intergovernmental Panel on Climate Change, *[Solomon, S., D. Qin, M. Manning, Z. Chen, M. Marquis, K.B. Averyt, M.Tignor and H.L. Miller (eds.)]. Cambridge University Press, Cambridge, United Kingdom and New York, NY, USA.*

Sassen, K., and S. Benson (2001), A midlatitude cirrus cloud climatology from the facility for atmospheric remote sensing. Part II: Microphysical properties derived from lidar depolarization, *Journal of the Atmospheric Sciences*, *58*(15), 2103-2112, doi:10.1175/1520-0469(2001)058<2103:amcccf>2.0.co;2.

Stephens, G. L. (2005), Cloud feedbacks in the climate system: A critical review, *Journal of Climate*, *18*(2), 237-273, doi:10.1175/jcli-3243.1.

Stephens, G. L., et al. (2002), The cloudsat mission and the a-train - A new dimension of space-based observations of clouds and precipitation, *Bulletin of the American Meteorological Society*, *83*(12), 1771-1790, doi:10.1175/bams-83-12-1771.

Su, J., J. Huang, Q. Fu, P. Minnis, J. Ge, and J. Bi (2008), Estimation of Asian dust aerosol effect on cloud radiation forcing using Fu-Liou radiative model and CERES measurements, *Atmospheric Chemistry and Physics*, *8*(10), 2763-2771.

Thorsen, and Q. Fu (2015), Automated Retrieval of Cloud and Aerosol Properties from the ARM Raman Lidar. Part II: Extinction, *Journal of Atmospheric and Oceanic Technology*, *32*(11), 1999-2023, doi:10.1175/jtech-d-14-00178.1.

Thorsen, Q. Fu, and J. Comstock (2011), Comparison of the CALIPSO satellite and ground-based observations of cirrus clouds at the ARM TWP sites, *Journal of Geophysical Research-Atmospheres*, *116*, doi:10.1029/2011jd015970.

Thorsen; Fu, Q. N., Rob K.; Turner David D.; Comstock Jennifer M. (2015), Automated

Retrieval of Cloud and Aerosol Properties from the ARM Raman Lidar. Part I: Feature Detection, *JOURNAL OF ATMOSPHERIC AND OCEANIC TECHNOLOGY*, *32*(11), 1977-1998, doi:10.1175/JTECH-D-14-00150.1.

Tomasi, C., and R. Manduchi (1998), Bilateral Filtering for Gray and Color Images, *IEEE International Conference on Computer Vision, Bombay, India*, doi:10.1109/ICCV.1998.710815.

Wang, Z., and K. Sassen (2001), Cloud type and macrophysical property retrieval using multiple remote sensors, *Journal of Applied Meteorology*, *40*(10), 1665-1682, doi:10.1175/1520-0450(2001)040<1665:ctampr>2.0.co;2.

Williams, K. D., and M. J. Webb (2009), A quantitative performance assessment of cloud regimes in climate models, *Climate Dynamics*, *33*(1), 141-157, doi:10.1007/s00382-008-0443-1.

Yan, H. R., J. P. Huang, P. Minnis, Y. H. Yi, S. Sun-Mack, T. H. Wang, and T. Y. Nakajima (2015), Comparison of CERES-MODIS cloud microphysical properties with surface observations over Loess Plateau, *Journal of Quantitative Spectroscopy & Radiative Transfer*, *153*, 65-76, doi:10.1016/j.jqsrt.2014.09.009.

Yuan, J., Q. Fu, and N. McFarlane (2006), Tests and improvements of GCM cloud parameterizations using the CCCMA SCM with the SHEBA data set, *Atmospheric Research*, *82*(1-2), 222-238, doi:10.1016/j.atmosres.2005.10.009.

Cloud Type	Performance (%)	Cloud Mask Confidence Level			
		≥10	≥20	≥30	≥40
Strong	False positive	0.048	0.044	0.009	0
	Failed negative	0.244	0.244	0.244	0.244
Moderate	False positive	0.103	0.103	0.063	0
	Failed negative	0.229	0.229	0.229	100
Weak	False positive	0.007	0.006	0.003	0
	Failed negative	9.774	96.788	100	100

Table 1. Summary of false positives and failed negatives for hypothetical strong, moderate and weak cloud cases in Fig.4 a1, a2, and a3, respectively.

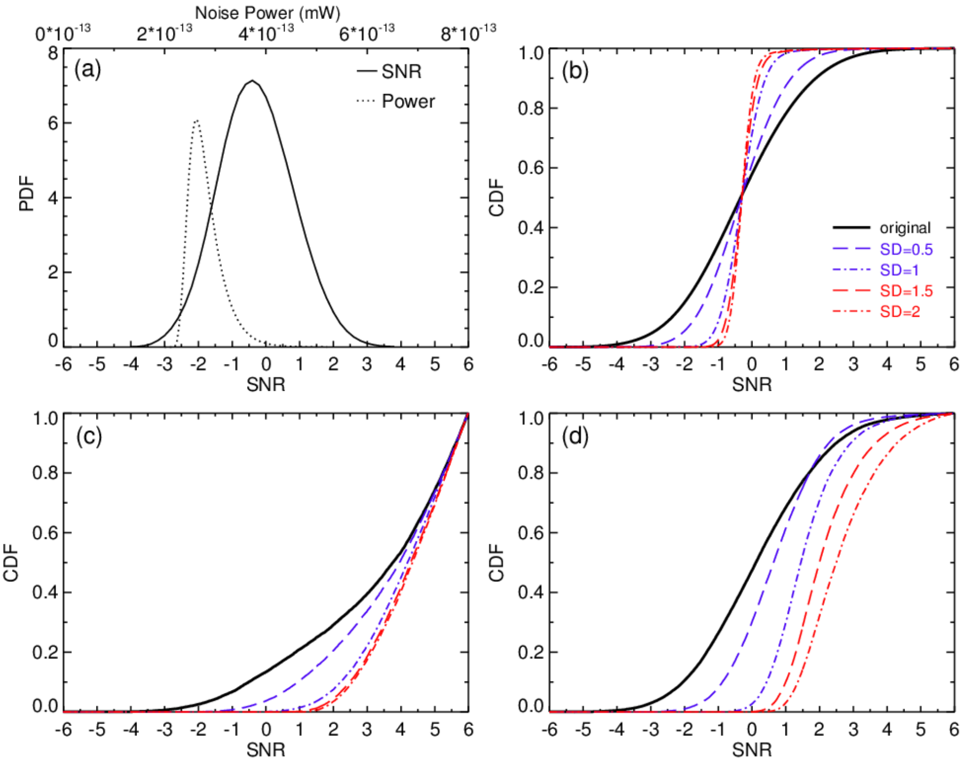

Figure 1. (a) Probability distribution function (PDF) of the noise power and SNR from the KAZR observations in a clear day of January 21, 2014. (b) Cumulative distribution function (CDF) of original and convolved SNR for the noise from the clear day. (c) and (d) CDF of original and convolved SNR from a cloudy case of January 4, 2014 for range gates inside and outside the cloud adjacent to the cloud boundary, respectively.

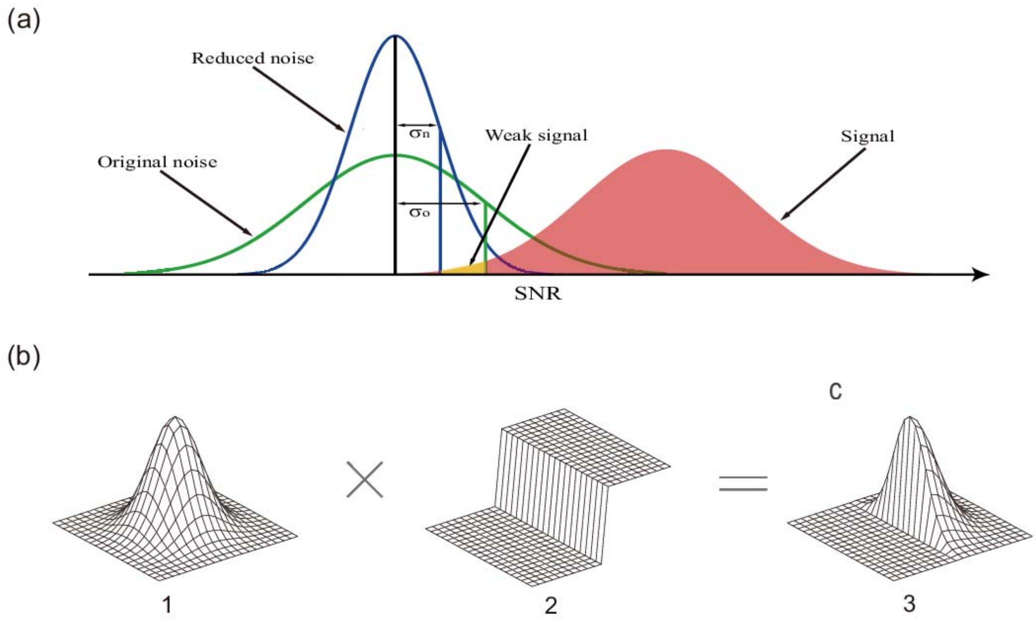

Figure 2. (a) comparison of original noise, reduced noise and hydrometeor signal distributions. (b) Illustration of the bilateral filtering process. (b1) Gaussian kernel distribution in space. (b2) δ function. (b3) Bilateral kernel by combining Gaussian kernel with δ function.

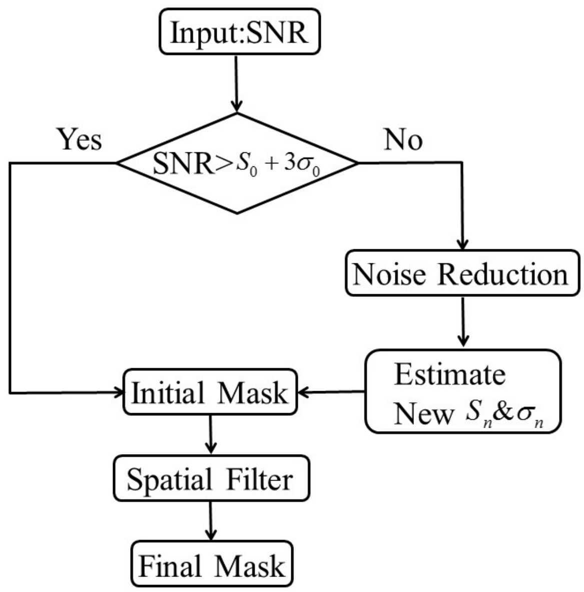

Figure 3. Schematic flow diagram for hydrometeor detection method.

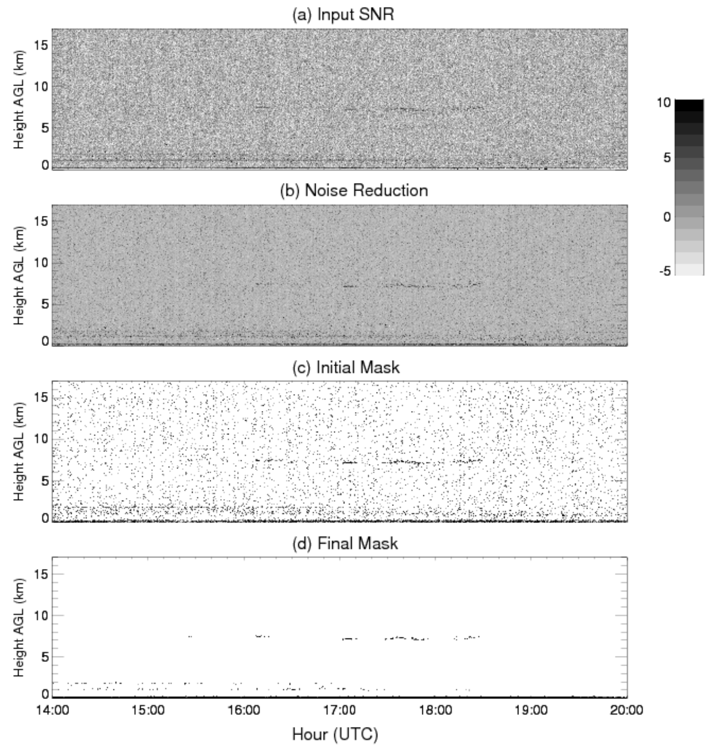

584 Figure 4. Illustration of the steps of the detection method using the real data of January

585 8th, 2014.

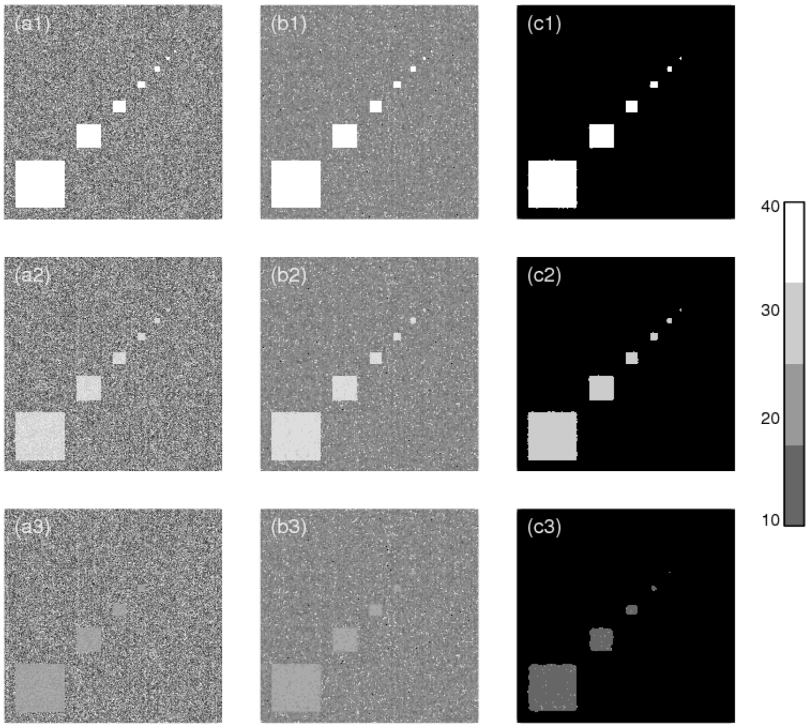

Figure 5. Panels a_1, a_2 and a_3 are three "square clouds" that have strong, moderate and weak SNR values with random Gaussian noise used to test the detection method. Panels b_1, b_2 and b_3 are SNR distributions after convolving the data with a bilateral kernel. Panels c_1, c_2 and c_3 are the final cloud mask filtered by the spatial filter.

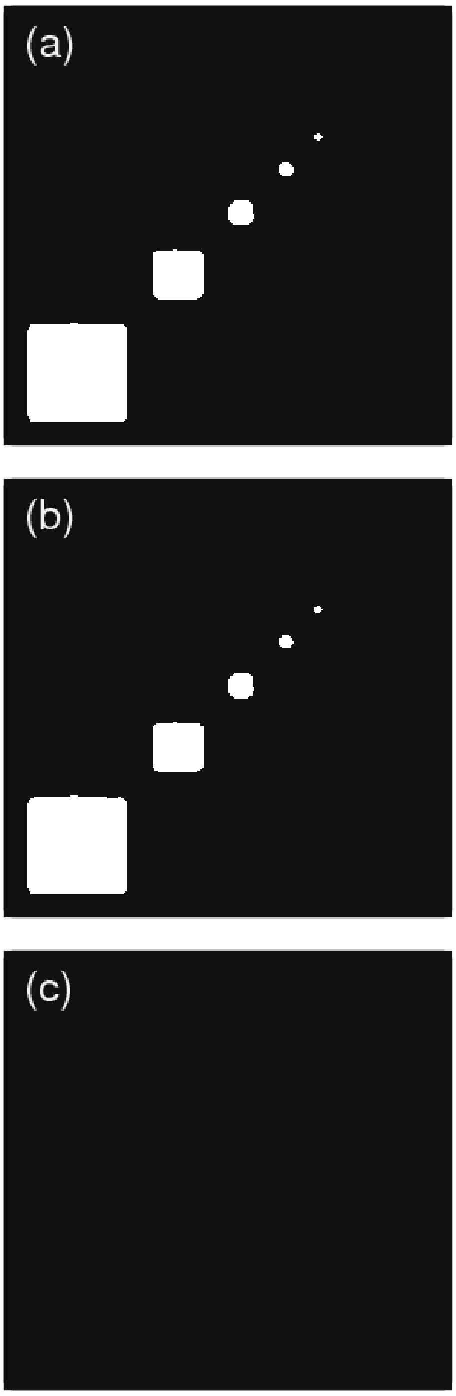

Figure 6. Cloud mask without applying noise reduction and central pixel weighting. (a), (b), (c) are for the targets with strong, moderate and weak SNR, respectively, from Fig. 4 a1, a2, and a3.

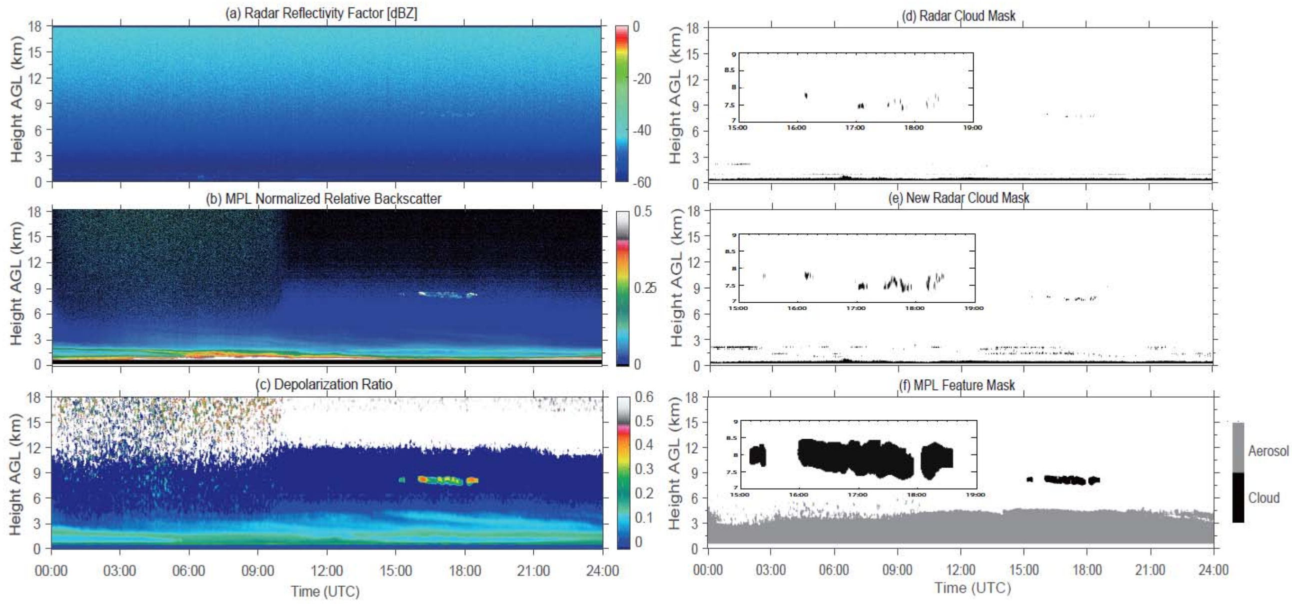

Figure 7. One-day example of radar- and lidar-observed cirrus cloud at the SACOL on January 8, 2014. (a) KAZR reflectivity. (b) MPL normalized backscatter intensity (c)MPL Depolarization Ration (d) radar cloud mask derived by the ARM operational algorithm. (e) radar cloud mask derived by our new method. (f) MPL feature mask. Three windows in (d), (e), (f) show the zoom-in views of cirrus masks.

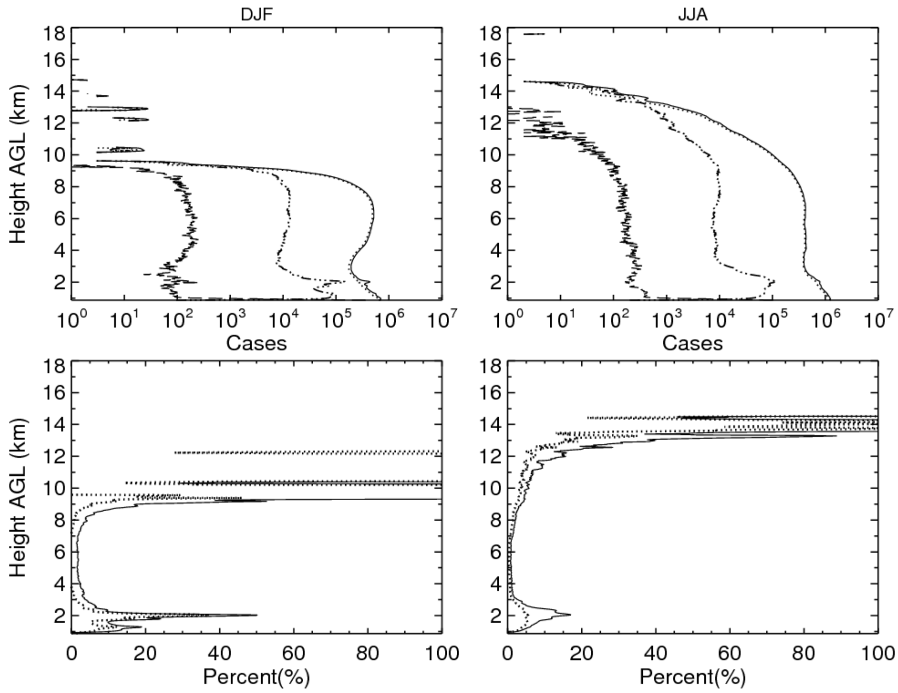

Figure 8. The upper panel shows the number of occurrences of the detected hydrometeor range bins from the two methods with the confusion matrix. The solid line represents the results derived from our new method. The dot line represents the range gate number that are detected as signals by both methods. The dashed line is the number of range gates detected as noise by our method but signal by ARM. The dot-dash line is the increased range gates from our method. The lower two panels demonstrate the increased percentage of hydrometeor bins from our new method comparing to the ARM operational method. The solid line is calculated by applying both noise reduction and central-pixel weighting schemes, while the dashed line is calculated by only applying the central-pixel weighting scheme in our detection method.

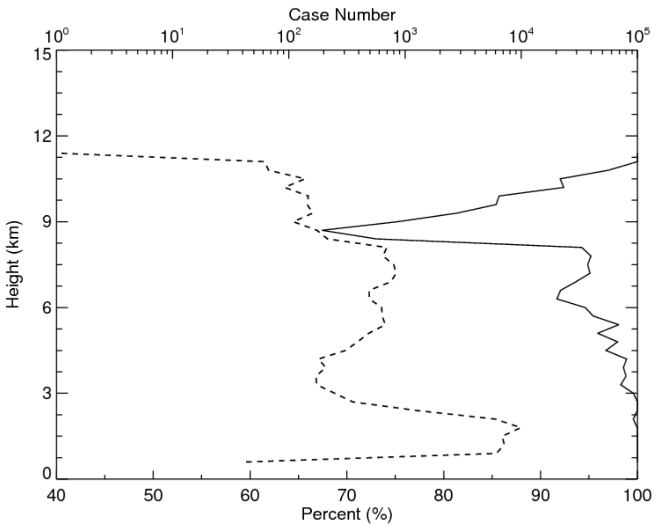

Figure 9. A comparison of the increased detections with the MPL observations. The solid line is the percentage of increased detections seen by both KAZR with our method and MPL as compared with the total increased detections. The dot line is the number of increased detections.

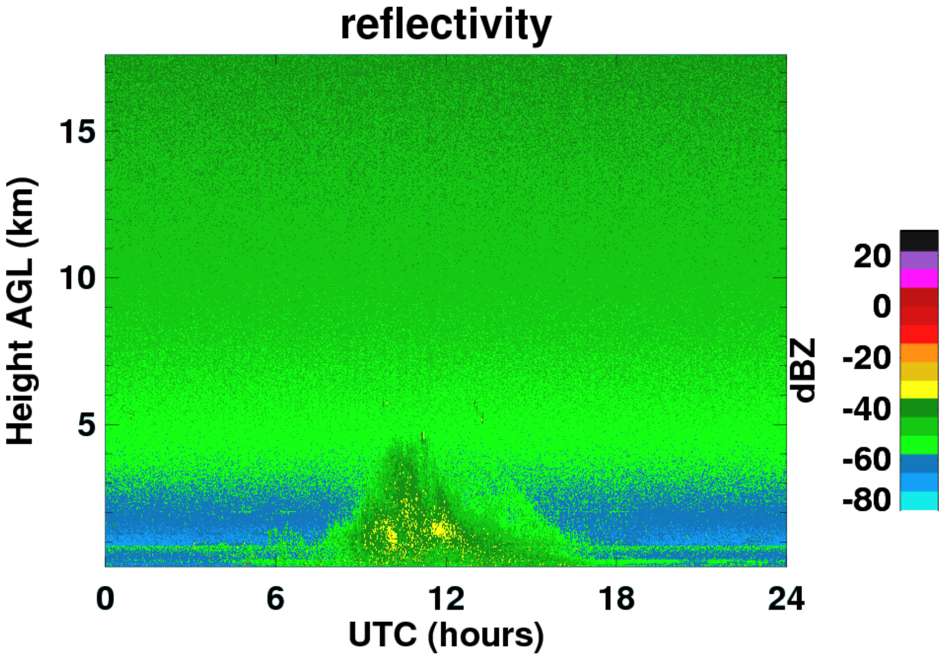

Auxiliary Figure 1. A dust event observed on January 29th, 2014. The morphology and power level of the return signal is apparent not for a cloud from the surface to the height of 5 km between 0800 to 1600 UTC.